# An Electro-Chemo-Mechanic Model Resolving Delamination between Components in Complex Microstructures of Solid-State Batteries

Christoph P. Schmidt,[1,*,z] Stephan Sinzig,[1,2,*] and Wolfgang A. Wall[1,2]

[1]*TUM School of Engineering and Design, Department of Engineering Physics and Computation, Institute for Computational Mechanics, Technical University of Munich, Boltzmannstraße 15, 85748 Garching bei München, Germany*
[2]*TUMint.Energy Research GmbH, Lichtenbergstraße 4, 85748 Garching bei München, Germany*

A novel approach is presented to model delamination and recontacting at internal interfaces of three-dimensional resolved microstructures of solid-state batteries. To resolve the effect of delaminations, we incorporate the consistent enforcement of contact constraints at those interfaces using Nitsche's method. The model incorporates charge, mass, and momentum conservation to consider electrochemistry, solid mechanics, and their interaction. After introducing and verifying the model, we examine various scenarios to quantify the effect of delaminations at the electrode-solid electrolyte interface on cell performance. The simulations show that increased mechanical stack pressure during cycling mitigates delamination tendencies at the electrode-solid electrolyte interface. Consistent with existing literature, the simulations demonstrate that delaminations increase the internal resistance and reduce the amount of transferred charge. In contrast to experimental analyses, the presented model allows quantitative and in-depth investigations of delamination effects. Furthermore, our analysis of two cell concepts—one assembled in the discharged state and another assembled in the charged state—indicates that half-cells assembled in an initial state from which the active material shrinks in volume upon first charge or discharge show a higher delamination risk at the electrode-solid electrolyte interface. The study highlights the critical relationship between solid mechanics and electrochemistry in consideration of delamination phenomena in solid-state batteries, offering valuable insights for optimizing battery design and performance.

Due to intensive research, the energy and power density of batteries has increased significantly in recent years. However, lithium-ion batteries with liquid electrolytes have almost reached their physicochemical limit concerning energy density.[1] Solid-state batteries (SSB) are a promising technology to overcome this limit, especially if the lithium metal anode or other high-capacity anode materials like silicon are enabled. Yet, these systems require intensive research as the interaction effects of solid mechanics and electrochemistry are, to date, poorly understood[2] but are of great importance for their performance. The delamination of active material and solid electrolyte at both the anode and cathode side is a phenomenon that is frequently reported in the literature. At the anode side, void formation due to lithium stripping from the lithium metal anode is often documented for systems with oxide-based[3,4] and sulfide-based[5–8] solid electrolytes. It is commonly observed that delaminations result in increased cell resistance due to a reduced active interface area, which leads to current constrictions. This effect can be moderated by increasing the stack pressure as shown in, e.g. Refs. 5, 8. Furthermore, the composite cathode can also be affected by the delamination of the active material and the solid electrolyte. This is usually attributed to the volume changes of the cathode active materials during cycling, resulting in accumulating voids at the interface of active material and solid electrolyte, as demonstrated in Refs. 9–12.

Several computational models are being developed that include these phenomena and support the development of SSB through systematic analysis. However, since the physical effects relevant to the SSB are challenging, both from the modeling and numerical point of view, and their solution is computationally demanding, numerous simplifications like spatial homogenization are often applied. Those simplifying assumptions can significantly limit the validity and predictive character of the models. In Ref. 13 a one-dimensional Newman model has been proposed to include the effect of contact area loss in a phenomenological manner. Several publications investigate SSB by reduction to two-dimensional geometries analyzing the void formation at the interface of lithium metal anode and solid electrolyte[14–19] or the delamination of cathode active material and solid electrolyte upon cycling.[20–22] Moreover, models analyzing three-dimensional geometries have been presented but only applied to one isolated active material particle embedded into a solid electrolyte matrix.[23] Others investigated resolved microstructures but analyzed the delamination only by evaluating a so-called debonding index, neglecting the interaction on the electrochemistry that no flux of charges or mass can be transferred over delaminated interfaces.[24] In Ref. 25 interface effects are analyzed in detail, but the consideration of solid mechanics, i.e. the calculation of deformations and mechanical stresses, is not assessed. Instead, the interfaces of the resolved microstructures that are delaminated are specified as input regardless of the actual mechanical state.

In this work, we propose a computational model to investigate the effect of delamination and potential recontacting at the internal interfaces of SSB, which is integrated into a three-dimensional model incorporating electrochemistry and solid mechanics on resolved microstructures. The effect of delaminations is introduced by consistently enforcing the constraints originating from contact mechanics using Nitsche's method. The model is based on nonlinear continuum mechanics and can account for large deformations originating from lithiation-dependent volume changes of the active materials due to (de-)lithiation while consistently accounting for mass and charge conservation. We solve the coupled equation of the fields in a monolithic fashion to increase the robustness of the solver for the highly nonlinear system and the computational efficiency of the algorithm. Application of advanced physics-oriented block preconditioning of the linear system of equation combined with the full MPI-parallelization of our implementation allows to close the gap in the literature to solve the complex nonlinear model, including the effect of delamination on complex microstructures of SSB.

As this work focuses on delamination and recontacting at internal interfaces, we first discuss the relevance of further effects related to the electro-chemo-mechanical interaction at internal interfaces. We start with evaluating the effect of solid mechanics on the reaction kinetics at the interface. The mechanical stress state at the interface influences the electrochemical equilibrium via the open circuit voltage (OCV) and the reaction rate by the exchange current density. For the OCV, Ref. 26

*Electrochemical Society Student Member
zE-mail: christoph.schmidt@tum.de

measured a dependence of 1 mV/100 MPa experimentally. In Ref. 27 an elaborate model to incorporate this effect is presented. They also refer to the aforementioned experimentally determined value and report that their modeling results in a value of the same magnitude, i.e. 3.6 mV/100 MPa. Since in this work, we vary the external pressure from 50 to 70 MPa, i.e. by 20 MPa, we expect that the influence of the variation of the external stack pressure on the OCV is clearly below 1 mV. By anticipating the relevant voltage range for cycling being between 2.8 and 4.2 V, the influence of the mechanical stresses on the OCV is less than one per mil compared to the cycling voltage range and, therefore, negligible. Furthermore, a model for the effect of mechanical stresses on the exchange current density is suggested in Ref. 27. By applying their model for single ion conductor electrolytes and storage particle electrode materials using the anticipated variation in external mechanical stack pressure of 20 MPa, we obtain a deviation of the exchange current density of approximately 1.4% between the exchange current density of the lowest and highest stack pressure. Thus, we also consider this effect to be negligible for the presented examples. Finally, we evaluate whether adhesion effects play an important role concerning the delamination of active material and solid electrolyte. Therefore, we present information from the literature on the adhesion strengths of such interfaces. Unfortunately, the available studies are scarce. Thus, we also report values of material combinations that are relevant in SSB but will not be investigated in this work, as well as data for cells with liquid electrolytes. In Ref. 28 the adhesion strength for different compositions of composite cathodes composed of the lithium nickel manganese cobalt oxide (NMC622) cathode active material, a chlorine argyrodite solid electrolyte, a hydrogenated acrylonitrile-butadiene rubber (HNBR) binder, and C65 carbon black with different mass loadings are measured with a maximum tensile stress of 412 kPa before delamination was observed. Adhesion strengths of approximately 30 kPa and 540 kPa are reported for the interface of $Li_4Ti_5O_{12}$ (LTO) and the garnet-type $Li_7La_3Zr_2O_{12}$ (LLZO) solid electrolyte when using polyvinylidene fluoride (PVDF) binder with a mixture of tetrahydrofuran (THF) and toluene solvent, and polyvinyl butyral (PVB) binder with terpineol solvent, respectively.[29] Moreover, Ref. 30 correlated interface resistance and adhesion strength for the Li-LLZO interface. They obtained an adhesion strength of 1.1 kPa for the interface with the highest interface resistance and an adhesion strength of 8 MPa for the interface with the lowest interface resistance. There are similar values of the adhesion strengths reported for lithium-ion batteries with liquid electrolyte with a maximum value of 2.3 MPa in Ref. 31 and a range of 200 kPa to 1.2 MPa in Ref. 32. We expect the highest relevance for the adhesion strength reported in Ref. 28 with a maximum of 412 kPa, as the material combination investigated therein is closest to the one in this work. In the result section we will show based on this literature review, that it is justified to omit adhesion effects at the solid-solid interface.

The structure of the paper is as follows: First, the model, including all governing equations, is presented before we comment on selected numerical aspects concerning the finite element formulation. Afterward, we verify the proposed model by comparing the numerical results to an analytic solution. The model is further verified by showing that the conservation of mass is fulfilled before applying it to different scenarios to gain insights into the complex interaction of solid mechanics and electrochemistry with a focus on the delamination effect at the interface of electrode and solid electrolyte. Finally, we summarize the presented work and propose interesting topics concerning future SSB development inspired by the insights obtained from the novel model.

## Problem Definition

Delaminations of electrodes and electrolytes in SSB during cycling are a highly nonlinear interaction effect of solid mechanics and electrochemistry since, for example, deformations are driven by the state of charge of the active materials, and conduction paths change drastically once a gap opens. Consequently, solid mechanics,
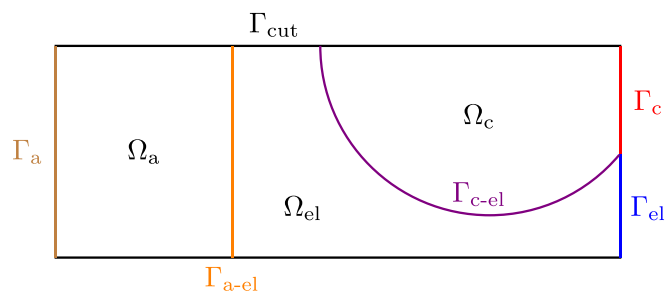


**Figure 1.** Schematic sketch of the computational domain.

electrochemistry, and their mutual interaction are considered in the presented model. To properly define the problem setup, we show a schematic sketch depicting all domains and interfaces inside an SSB relevant to the modeling approach. Then, the equations applied to the bulk domains are presented. Finally, we elaborate on the interface modeling equations and the boundary and initial conditions.

***Geometric definitions.***—While the approach presented in this paper can be applied to a large variety of cases, it will be demonstrated and investigated using an SSB cell that consists of a lithium metal anode, a solid electrolyte separator, and a composite cathode. A schematic of the cell is shown in Fig. 1. It comprises an anode domain $\Omega_a$, a homogenized solid electrolyte domain $\Omega_{el}$, and a cathode domain $\Omega_c$ only representing the cathode active material. For a more convenient notation, the electrode domain is introduced as $\Omega_{ed} = \Omega_a \cup \Omega_c$. The interface of anode and electrolyte is denoted by $\Gamma_{a-el}$, whereas the interface between cathode and electrolyte is depicted as $\Gamma_{c-el}$. Furthermore, we define the boundary of the anode and the anode-side current collector using $\Gamma_a$. Moreover, the boundaries of the cathode and the electrolyte with the cathode-side current collector are depicted by $\Gamma_c$ and $\Gamma_{el}$, respectively. Finally, $\Gamma_{cut}$ symbolizes the surfaces of a "computational cut" in lateral directions to obtain a representative section of the real battery. The current collectors are not explicitly modeled because they do not significantly affect the investigated scenarios.

Please note that the solid electrolyte microstructure inside an SSB is generally more complex in reality as remaining voids or additional phases like binder or carbon black are omitted in the homogenized solid electrolyte domain investigated in this work. Recent numerical studies[33,34] aim to investigate the influence of those effects by deducing effective bulk conductivities and interface properties through analysis of artificial microstructures that three-dimensionally resolve those features. Then, they analyze the implications on the cathode dynamics using Newman-type models. In contrast, geometric details like voids can be incorporated into our presented model due to the three-dimensional resolution. If only the overall electrochemical effect but not the local resolution is desired, the material properties can be replaced by the respective effective properties as deduced in the publications mentioned above.

***Bulk equations.***—As this work focuses on delamination phenomena occurring at the interfaces of electrodes and electrolyte, we do not repeat all details on the bulk formulation. Instead, we summarize the bulk equation that have been presented and analyzed in detail in our previous work[35]

$$\rho_0 \ddot{\boldsymbol{u}} = \nabla_X \cdot (\boldsymbol{F} \cdot \boldsymbol{S}) + \boldsymbol{b}_0 \quad \text{in } \Omega_0, \quad [1]$$

$$\boldsymbol{F} = \boldsymbol{F}_{el} \cdot \boldsymbol{F}_{gr} \quad \text{in } \Omega_0, \quad [2]$$

$$\boldsymbol{S} = 2 \det(\boldsymbol{F}_{gr}) \boldsymbol{F}_{gr}^{-1} \cdot \frac{\partial \Psi_{el}}{\partial \boldsymbol{C}_{el}} \cdot \boldsymbol{F}_{gr}^{-T} \quad \text{in } \Omega_0, \quad [3]$$

$$\Psi_{el} = \alpha[\mathrm{tr}(\boldsymbol{C}_{el}) - 3] + \frac{\alpha}{\beta}[\det(\boldsymbol{C}_{el})^{-\beta} - 1] \qquad \text{in } \Omega_0, \qquad [4]$$

$$0 = \nabla\cdot(-\sigma\nabla\Phi) \qquad \text{in } \Omega_{ed}, \qquad [5]$$

$$0 = \nabla\cdot(-\kappa\nabla\Phi) \qquad \text{in } \Omega_{el}, \qquad [6]$$

$$0 = \left.\frac{\partial c}{\partial t}\right|_X + c\nabla\cdot\dot{\boldsymbol{u}} - \nabla\cdot(D\nabla c) \qquad \text{in } \Omega_{ed}, \qquad [7]$$

$$0 = \left.\frac{\partial c}{\partial t}\right|_X + c\nabla\cdot\dot{\boldsymbol{u}} \qquad \text{in } \Omega_{el}, \qquad [8]$$

$$\boldsymbol{F}_{gr} = \boldsymbol{I} + \left[g\det(\boldsymbol{F})\frac{n_a - n_a^0}{V}\right]\boldsymbol{g}\otimes\boldsymbol{g} \qquad \text{in } \Omega_a, \qquad [9]$$

$$\boldsymbol{F}_{gr} = \left(\frac{f(\chi) + 1}{f(\chi_0) + 1}\right)^{1/3}\boldsymbol{I} \qquad \text{in } \Omega_c. \qquad [10]$$

Equation 1 represents the conservation of linear momentum employing the mass density in the reference configuration $\rho_0$, the second temporal derivative of the displacements $\ddot{\boldsymbol{u}}$, the material divergence operator $\nabla_X\cdot$, the deformation gradient $\boldsymbol{F}$, the second Piola–Kirchhoff stress tensor $\boldsymbol{S}$, and a body force per unit volume in reference configuration $\boldsymbol{b}_0$. The volumetric changes of the electrodes due to (de-)lithiation are modeled based on a multiplicative split of the deformation gradient (cf Eq. 2) into a purely elastic deformation $\boldsymbol{F}_{el}$ and a deformation caused by the volumetric changes of the active materials $\boldsymbol{F}_{gr}$. The assumption that only elastic strains result in mechanical stresses combined with applying a hyperelastic material law results in the constitutive equation for the solid mechanics presented in Eq. 3. It uses the elastic strain energy function $\Psi_{el}$ and the elastic right Cauchy–Green tensor $\boldsymbol{C}_{el} = \boldsymbol{F}_{el}^T\cdot\boldsymbol{F}_{el}$. While arbitrary elastic strain energy functions can be used in the presented model, we use the Neo–Hooke formulation as shown in Eq. 4 throughout this work. The material parameters $\alpha = E/[4(1 + \nu)]$ and $\beta = \nu/(1 - 2\nu)$ are calculated from the Young's modulus $E$ and the Poisson's ratio $\nu$. The Cauchy stress tensor $\boldsymbol{\sigma}$ is required to evaluate the contact mechanics presented later. It is obtained by the mapping $\boldsymbol{\sigma} = (\det\boldsymbol{F})^{-1}\boldsymbol{F}\cdot\boldsymbol{S}\cdot\boldsymbol{F}^T$. Furthermore, the conservation of charge is considered by Eqs. 5 and 6 with the electric potential $\Phi$ as well as the electronic and ionic conductivity $\sigma$ and $\kappa$, respectively. Finally, Eqs. 7 and 8 represent the conservation of mass evaluated on a domain that deforms with $\boldsymbol{u}$ to account for large deformations using the lithium(-ion) concentration $c$ and the diffusion coefficient $D$ as well as the deformation velocity $\dot{\boldsymbol{u}}$. Please note that two reasonable assumptions have been made to derive these specific equations for the conservation of charge and mass. First, the local electroneutrality condition holds inside the whole battery domain, and second, the solid electrolyte is a single ion conductor, represented by a transference number of 1. Moreover, we remark that the conductivity and the diffusion constants are unaffected by strain and thus remain isotropic and that the effect of stress gradients is neglected. We also want to point out that the bulk equations of solid mechanics are formulated in the material or undeformed configuration $\Omega_0$. In contrast, the conservation equations of electrochemistry are formulated in the spatial or deformed configuration $\Omega = \Omega_{ed}\cup\Omega_{el}$. Since the focus of this work is the investigation of the delamination behavior at the composite cathode, we do not resolve the surface deposition and dissolution at the lithium metal anode but instead homogenize the change in volume by using an anisotropic volumetric growth (cf Eq. 9) in growth direction $\boldsymbol{g}$, i.e. the through-thickness direction of the battery cell. A meaningful parameterization of the growth factor $g = M_{Li}/\rho_{Li}$ is obtained as the division of the molar mass $M_{Li}$ and the mass density $\rho_{Li}$ of lithium. The anisotropic growth law is completed by the amount of substance of

lithium inside the anode $n_a = \int_{\Omega_a} c\,dV$ and the associated amount of substance at the beginning of the simulation $n_a^0$ as well as the current volume $V$. The volume change of the cathode active material is modeled to be isotropic as presented in Eq. 10 since, throughout this work, it is applied for secondary NMC particles whose primary particles can be assumed to be randomly distributed. It is parameterized by the polynomial $f(\chi) = \Delta V/V_{ref} = (V(\chi) - V(\chi_{ref}))/V(\chi_{ref})$ being a fit of published data of the volume change as a function of the lithiation state $\chi = c\,\chi_{max}\det(\boldsymbol{F})/c_{max}$, where the maximum concentration of lithium inside the electrode is denoted by $c_{max}$ and the corresponding lithiation state by $\chi_{max}$. For further details on the bulk model, we refer to Ref. 35.

***Interface equations.***—The electrode-electrolyte interface $\Gamma_{ed-el} = \Gamma_{a-el}\cup\Gamma_{c-el}$ is divided into two areas. In the first part of the interface, we assume that no delamination occurs, i.e. the adjacent bodies are always in contact at their common interface. This area is called the *mesh tying* interface $\Gamma_{mt}$, or $\gamma_{mt}$ in the deformed state. A delamination of the bodies and subsequent recontacting can occur in the second part of the interface. This is called the *contact* interface $\Gamma_{ct}$, or $\gamma_{ct}$. To ease the notation, we restrict ourselves to scenarios where only two bodies are in contact (cf Fig. 2), while the model and implementation can handle an arbitrary number of bodies. We denote the first body with superscript $*^{(1)}$ and the second body with superscript $*^{(2)}$. Subsequently, we show the mathematical formulation for the solid mechanics and the electrochemistry for the aforementioned interfaces.

*Conservation of momentum at the interface.*—First, we describe the mathematical model for the *mesh tying* interface. Since we do not allow delamination of the bodies at this interface, the following kinematic constraint is applied

$$\boldsymbol{u}^{(1)} = \boldsymbol{u}^{(2)} \qquad \text{on } \gamma_{mt}, \qquad [11]$$

to ensure that both bodies remain in contact.

To mathematically describe the *contact* interface, we introduce a smooth mapping $\chi_t$ between the interface $\gamma_{ct}^{(1)}$ and the interface $\gamma_{ct}^{(2)}$ at a time instant $t$ as

$$\chi_t(\boldsymbol{x}^{(1)}, t):\ \gamma_{ct}^{(1)} \rightarrow \gamma_{ct}^{(2)},\ \boldsymbol{x}^{(1)} \mapsto \boldsymbol{x}^{(2)} \qquad \text{on } \gamma_{ct}. \qquad [12]$$

As depicted in Fig. 2, this mapping projects any point $\boldsymbol{x}^{(1)}$ on the contact interface of body (1) along the outward-pointing unit
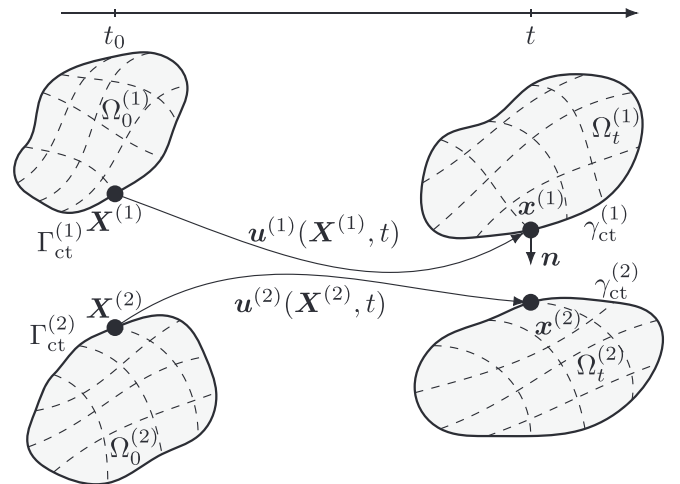


**Figure 2.** Notation and kinematics to depict the contact interaction between two deformable bodies. The left part shows a configuration at time $t_0$ where the two bodies are not in contact. The right part illustrates the deformed bodies at time $t$ in contact but with a virtual separation for illustration purposes.

normal $\boldsymbol{n}^{(1)}$, or simply $\boldsymbol{n}$, to the contact interface $\gamma_{ct}^{(2)}$ on body (2). The normal gap $g_n$ is a kinematic measure to evaluate if two bodies are in contact

$$g_n(\boldsymbol{x}^{(1)}) = -\boldsymbol{n}\cdot[\boldsymbol{x}^{(1)} - \boldsymbol{x}^{(2)}] \quad \text{on } \gamma_{ct}. \quad [13]$$

It is zero at the locations where the bodies are in contact and positive everywhere else. As bodies cannot penetrate each other, the normal gap cannot be negative ($g_n \geqslant 0$). Remember that $\gamma_{ct}$ denotes the interface where the two bodies *are* or *can be* in contact. At the surface of the body $k$ the traction vector $\boldsymbol{t}^{(k)}$ is calculated by Cauchy's stress theorem as

$$\boldsymbol{t}^{(k)} = \boldsymbol{\sigma}^{(k)}\cdot\boldsymbol{n}^{(k)} \quad \text{on } \gamma_{ct}. \quad [14]$$

Moreover, the balance of linear momentum in the contact zone requires

$$\boldsymbol{t}^{(1)} = -\boldsymbol{t}^{(2)} \quad \text{on } \gamma_{ct}. \quad [15]$$

The traction vector $\boldsymbol{t}$ is split into the normal contact traction $p_n$ calculated as

$$p_n = \boldsymbol{n}\cdot\boldsymbol{t} \quad \text{on } \gamma_{ct}, \quad [16]$$

and a tangential contact traction $\boldsymbol{t}_t = \boldsymbol{t} - p_n\boldsymbol{n}$. As we do not account for adhesion in this work, the normal contact traction can only originate from compressive forces, i.e. $p_n \leqslant 0$. Without friction effects, the tangential contact traction has to vanish $\boldsymbol{t}_t = \boldsymbol{0}$. Consequently, the contact constraints for normal, frictionless contact without adhesive interface forces are given as

$$g_n \geqslant 0, \quad p_n \leqslant 0, \quad g_n p_n = 0 \quad \text{on } \gamma_{ct}, \quad [17]$$

representing the Hertz–Signiorini–Moreau conditions. Although we do not consider the effects of friction and adhesion in this work, the presented model could be extended to include such effects based on our previous work, including friction[36] and adhesion[37] effects.

*Conservation of charge and mass at the interface.*—For the electrochemical model, we take into account the conservation of charge and mass at the interface

$$i_l^{(1)} + i_l^{(2)} = 0, \quad [18]$$

$$j_l^{(1)} + j_l^{(2)} = 0, \quad [19]$$

with $l \in \{ct, mt\}$. Furthermore, the interface fluxes of charge $i^{(k)}$ and mass $j^{(k)}$ are calculated as follows

$$i^{(k)} = \boldsymbol{i}^{(k)}\cdot\boldsymbol{n}^{(k)}, \quad j^{(k)} = \boldsymbol{j}^{(k)}\cdot\boldsymbol{n}^{(k)}, \quad [20]$$

based on the outward-pointing unit normal $\boldsymbol{n}^{(k)}$ of body $k$ and the corresponding vector-valued flux densities of charge $\boldsymbol{i}^{(k)}$ and mass $\boldsymbol{j}^{(k)}$ that are calculated as

$$\boldsymbol{i} = -\sigma\nabla\Phi \quad \text{on } \partial\Omega_{ed}, \quad [21]$$

$$\boldsymbol{i} = -\kappa\nabla\Phi \quad \text{on } \partial\Omega_{el}, \quad [22]$$

$$\boldsymbol{j} = -D\nabla c \quad \text{on } \partial\Omega_{ed}, \quad [23]$$

$$\boldsymbol{j} = \frac{\boldsymbol{i}}{F} \quad \text{on } \partial\Omega_{el}, \quad [24]$$

with the Faraday constant $F$. Moreover, we employ the Butler–Volmer kinetics to model the interface flux

$$jF = i = i_0\left[\exp\left(\frac{\alpha_a F}{RT}\eta\right) - \exp\left(-\frac{(1-\alpha_a)F}{RT}\eta\right)\right], \quad [25]$$

using the exchange current density $i_0$, the anodic symmetry coefficient $\alpha_a$, the universal gas constant $R$, and the temperature $T$. The overvoltage $\eta$ describes the driving force for the charge transfer reaction at the interface and is calculated as

$$\eta = \Phi_{ed} - \Phi_{el} - \Phi_0. \quad [26]$$

It consists of the difference in electric potential at the electrode $\Phi_{ed}$ and the electrolyte $\Phi_{el}$. Furthermore, the half-cell open circuit voltage $\Phi_0$ referenced against pure lithium metal is considered.

The equations of this section are unconditionally evaluated at the *mesh tying* interface $\gamma_{mt}$ as the bodies are always in intimate contact, and a transfer of charge and mass is permanently possible. However, for the *contact* interface $\gamma_{ct}$, we must consider that charge and mass are only transferred if the bodies are in contact, i.e. the normal contact traction is negative $p_n < 0$. To incorporate this effect, the interface kinetics is set to zero if the bodies have separated using

$$j^{(k)}F = i^{(k)} = \begin{cases} i & \text{if } p_n < 0 \\ 0 & \text{else} \end{cases} \quad \text{on } \gamma_{ct}. \quad [27]$$

**Boundary conditions.**—The mass flux between the battery domains and the adjacent current collectors has to vanish since the current collectors are assumed to be impermeable to lithium(-ions)

$$\boldsymbol{j}\cdot\boldsymbol{n} = 0 \quad \text{on } \Gamma_a \cup \Gamma_c \cup \Gamma_{el}. \quad [28]$$

Furthermore, as only a representative part of the real battery is considered in the lateral directions, we apply symmetry conditions at those surfaces, resulting in neither flux of mass nor flux of charges across these boundaries

$$\boldsymbol{j}\cdot\boldsymbol{n} = 0 \quad \text{on } \Gamma_{cut}, \quad [29]$$

$$\boldsymbol{i}\cdot\boldsymbol{n} = 0 \quad \text{on } \Gamma_{cut}. \quad [30]$$

The electric potential is set to a reference value at the interface between cathode active material and cathode-side current collector

$$\Phi = 0 \quad \text{on } \Gamma_c. \quad [31]$$

To enable galvanostatic charging or discharging, an electrical current density $\hat{i}$ is prescribed at the interface between the anode and the current collector on the anode side

$$-\boldsymbol{i}\cdot\boldsymbol{n} = \hat{i} \quad \text{on } \Gamma_a. \quad [32]$$

It is formulated such that a positive value of $\hat{i}$ represents a charging and a negative value a discharge process. There is also no flux of charges across the electrolyte-current collector interface since the electrolyte is modeled to be an electrical insulator preventing the flux of electrons, and the current collectors are impermeable to lithium (-ions), as already mentioned above

$$\boldsymbol{i}\cdot\boldsymbol{n} = 0 \quad \text{on } \Gamma_{el}. \quad [33]$$

For the solid mechanics, Dirichlet and Neumann boundary conditions are applied as

$$\boldsymbol{u} = \hat{\boldsymbol{u}} \quad \text{on } \Gamma_u, \quad [34]$$

$$(F \cdot S) \cdot N = \hat{t} \qquad \text{on } \Gamma_\sigma. \qquad [35]$$

with the prescribed boundary displacements $\hat{u}$ and traction vector $\hat{t}$. Furthermore, to consider the mechanical stiffness $k$ of the environment of the battery, e.g. a cell housing or a measuring setup, a Robin-type boundary condition is applied in the normal direction

$$(F \cdot S) \cdot N = k(u \cdot N - u_k)N \quad \text{on } \Gamma_k, \qquad [36]$$

with a displacement offset in the normal direction $u_k$ enabling the application of a defined mechanical stack pressure during cycling.

***Initial conditions.***—A proper definition of the initial conditions is required to complete the initial boundary value problem setup. At the beginning of the simulations, the battery is assumed to be in static equilibrium

$$c = c_{ed}^0 \qquad \text{in } \Omega_{ed}, \qquad [37]$$

$$c = c_{el}^0 \qquad \text{in } \Omega_{el}, \qquad [38]$$

$$u = 0 \qquad \text{in } \Omega_0, \qquad [39]$$

$$\dot{u} = 0 \qquad \text{in } \Omega_0, \qquad [40]$$

with the initial lithium(-ion) concentration in the electrodes and the electrolyte $c_{ed}^0$ and $c_{el}^0$, respectively. As the charge conservation equations are stationary (cf Eqs. 5 and 6), no initial conditions for the electric potentials are necessary.

## Aspects of The Numerical Model

In this chapter, we focus on incorporating the interface constraints for the conservation of momentum. Since we use the finite element method to discretize in space, the strong form of the conservation of momentum is reformulated to the so-called weak form, which reads

$$\delta \mathcal{W}_u = \int_{\Omega_0} \rho_0 \ddot{u} \cdot \delta u \, d\Omega + \int_{\Omega_0} F \cdot S : \nabla_X \delta u \, d\Omega + \int_{\Omega_0} b \cdot \delta u \, d\Omega$$
$$- \int_{\Gamma_\sigma} \hat{t} \cdot \delta u \, d\Gamma - \int_{\Gamma_{int}} t \cdot \delta u \, d\Gamma = 0,$$
$$[41]$$

with the test functions $\delta u$. Here, the last term represents the surface traction term integrated over the internal interfaces $\Gamma_{int} = \Gamma_{mt} \cup \Gamma_{ct} = \Gamma_{a-el} \cup \Gamma_{c-el}$ of the battery.

To enforce the *mesh tying* constraint (cf Eq. 11), a Lagrange multiplier strategy is employed. Therefore, we introduce the Lagrangian multipliers $\lambda$ and the corresponding test functions $\delta\lambda$. Then, the following contribution is added to the weak form of the solid mechanics problem to enforce the *mesh tying* constraint

$$\delta \mathcal{W}_{mt} = \int_{\gamma_{mt}} \delta\lambda \cdot (u^{(1)} - u^{(2)}) + (\delta u^{(1)} - \delta u^{(2)}) \cdot \lambda \, d\gamma. \qquad [42]$$

For more details on the treatment of the *mesh tying* interface, we refer to our previous work.[35]

Next, the *contact* contributions are considered. Therefore, the last term in Eq. 41 is reformulated for the contact interface

$$- \int_{\Gamma_{ct}} t \cdot \delta u \, d\Gamma = - \int_{\gamma_{ct}^{(1)}} t^{(1)} \cdot \delta u^{(1)} \, d\gamma - \int_{\gamma_{ct}^{(2)}} t^{(2)} \cdot \delta u^{(2)} \, d\gamma, \qquad [43]$$

where we assume that the complete contact interface $\Gamma_{ct}$ consists of the contact interfaces of the two contacting bodies $\gamma_{ct}^{(1)}$ and $\gamma_{ct}^{(2)}$. We introduce the jump operator $[\![*]\!] = *^{(1)} - (*^{(2)} \circ \chi_t)$ expressing the difference of a quantity across the interface. The expression in

brackets $(*^{(2)} \circ \chi_t)$ symbolizes that a quantity $*^{(2)}$ on the interface of body (2) is projected to the corresponding interface of body (1) using the mapping introduced in Eq. 12. In combination with the balance of linear momentum at the contact interface (cf Eq. 15), we obtain

$$- \int_{\gamma_{ct}^{(1)}} t^{(1)} \cdot \delta u^{(1)} \, d\gamma - \int_{\gamma_{ct}^{(2)}} t^{(2)} \cdot \delta u^{(2)} \, d\gamma = - \int_{\gamma_{ct}^{(1)}} t^{(1)} \cdot [\![\delta u]\!] \, d\gamma. \quad [44]$$

Furthermore, a weighted jump operator $\{*\}_{\omega_s} = \omega_s *^{(1)} - (1 - \omega_s)(*^{(2)} \circ \chi_t)$ with a weighting factor $\omega_s$ is introduced. Please note that in the continuous setup $\{t\}_{\omega_s} = t$ holds due to the balance of linear momentum at the contact interface.

So far, the surface traction term for the contact interface has only been reformulated, but the contact constraints are not yet accounted for in the weak form. To incorporate the contact constraints, the Hertz–Signiorini–Moreau conditions in Eq. 17 are reformulated to a non-smooth equality constraint

$$\{p_n\}_{\omega_s} - [\{p_n\}_{\omega_s} + \gamma_n g_n]_- = 0, \qquad [45]$$

with a non-negative penalty parameter $\gamma_n \geqslant 0$ and an operator returning the negative part of the argument $[*]_- = \min[0, *]$ as shown in e.g. Refs. 38–41. The contact constraint is now enforced using Nitsche's method, which was introduced in Ref. 42 and first applied in the context of contact mechanics in Ref. 43 by adding the following contribution to the weak form

$$\delta \mathcal{W}_{ct} = \int_{\gamma_{ct}^{(1)}} (\{p_n\}_{\omega_s} - [\{p_n\}_{\omega_s} + \gamma_n g_n]_-) n$$
$$\cdot \left( [\![\delta u]\!] - \frac{\theta}{\gamma_n} \mathcal{D}\{p_n\}_{\omega_s}[\delta u] \right) d\gamma, \qquad [46]$$

with the directional derivative $\mathcal{D}*[\star]$ of quantity $*$ in direction $\star$ and a parameter $\theta \in \{-1, 0, 1\}$. The parameter $\theta$ can be used to obtain a symmetric variant for $\theta = 1$, a skew-symmetric variant for $\theta = -1$, and a non-symmetric variant with fewer terms for $\theta = 0$. The methods deviate in stability, where the skew-symmetric version is stable for all choices of $\gamma_n \geqslant 0$, whereas the other methods demand a lower bound for $\gamma_n$. The non-symmetric version with $\theta = 0$ is applied throughout this work since it is explicitly appealing in the context of coupled problems where the additional derivative can get cumbersome to derive. For an analysis of the different methods in the context of nonlinear thermo-elasto-plastic problems, we refer to Ref. 44. The choice of the penalty parameter $\gamma_n$ contained in the weak form of the contact constraint in Eq. 46 and the weighting factor $\omega_s$ is so far unspecified. Details on how we choose them throughout this work can be found in Appendix A.

## Results

The presented model, which incorporates the effect of delaminations and possible recontacting in SSB, is applied to different scenarios to verify the model and create new physical insights into how electrochemical phenomena interact with mechanical delamination. All presented simulations are performed using our inhouse multi-physics research code 4C.[45] If not stated differently, the simulations use one material setup, where the anode consists of lithium metal. Furthermore, the sulfidic solid electrolyte $\beta - Li_3PS_4$ ($\beta$–LPS) and the cathode active material $Li_xNi_{0.6}Mn_{0.2}Co_{0.2}O_2$ (NMC622) is used. The corresponding material parameters are listed in the appendix in Tables B·I to B·III. All simulations are performed at a temperature of 298 K.

***Verification of the outlined model.***—To verify the outlined model, we perform a so-called patch test to check the consistency of the model by comparing the results of the conservation of momentum and charge with the analytic solution. The verification is completed by showing that the model also fulfills the conservation of mass.
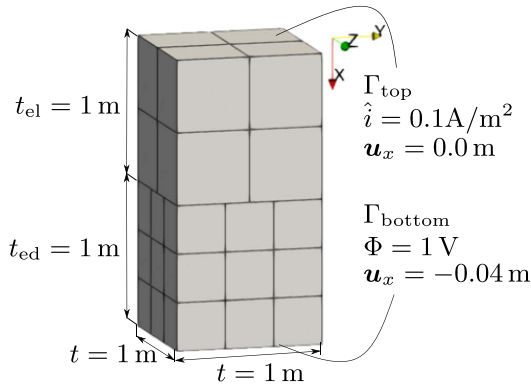
**Figure 3.** Geometry and boundary conditions of the patch test.

---

**Table I. Material parameters used for the patch test.**

**electrolyte cube:**

$\kappa = 1.0 \, \frac{\text{S}}{\text{m}}$, $E = 20 \, \text{Pa}$, $\nu = 0.3$

---

**electrode-electrolyte interface:**

$i_0 = 0.1 \, \frac{\text{A}}{\text{m}^2}$, $\alpha = 0.5$, $\Phi_0 = 0.3 \, \text{V}$

---

**electrode cube:**

$\sigma = 2.0 \, \frac{\text{S}}{\text{m}}$, $E = 20 \, \text{Pa}$, $\nu = 0.3$
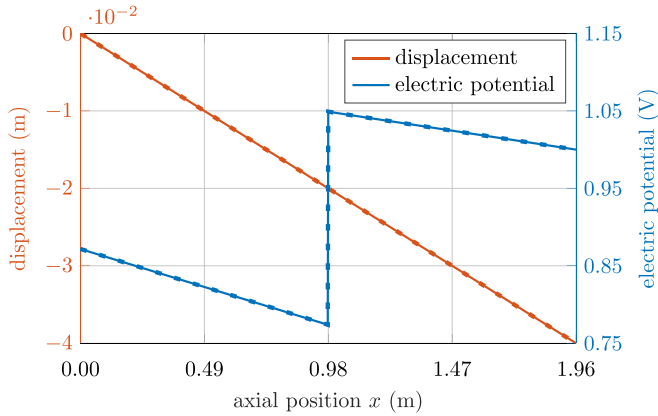
---



**Figure 4.** Comparison of the analytic solution (dashed line) and the simulation result (solid line) of the patch test for the displacement and the electric potential.

*Electro-chemo-mechanical contact patch test.*—For the electro-chemo-mechanical contact patch test, two blocks representing an electrode and a solid electrolyte domain are considered with non-conforming meshes at the interface as depicted in Fig. 3. As common for patch tests, a stationary scenario is investigated. Thus, we only analyze the conservation of momentum and charge, while the conservation of mass is checked later. A charge current of $0.1 \, \text{A/m}^2$ and a displacement in *x*-direction of 0 m are specified as boundary conditions at the top surface $\Gamma_{\text{top}}$ (cf Fig. 3). In addition, an electric potential of 1 V and a displacement in *x*-direction of $-0.04$ m is imposed at the bottom surface $\Gamma_{\text{bottom}}$. Moreover, lateral displacements in the *y*- and *z*-directions are set to 0 m at the surfaces of the body. A Neo-Hookean hyperelastic material model is used for both blocks. Since the patch test is not intended to depict a realistic scenario but rather to check the numerical consistency of the model, the material parameters listed in Table I are artificial and do not represent realistic materials. As the analytic solution is linear and hexahedral finite elements with linear shape functions can exactly

represent this analytic solution, a consistent method can reproduce this solution up to numerical tolerances. Consequently, we need to check whether the numerical results of the patch test agree with the analytic solution. Fig. 4 shows that the analytic solution depicted using dashed lines and the numerical result of the patch test visualized using solid lines match very well for the displacement and the electric potential. The displacement is linearly decreasing along the axial position. Furthermore, the electric potential shows a linear progression along the *x*-axis with a jump at the contact interface determined by the employed Butler–Volmer kinetics. Quantifying the deviation between the analytic and the numerical solution of quantity * using

$$\varepsilon_* = \frac{\int (* - *_{\text{analytic}})^2 \, d\Omega}{\int *_{\text{analytic}}^2 \, d\Omega}, \quad [47]$$

results in an error in the displacement solution of $\varepsilon_{\boldsymbol{u}} \approx 10^{-12}$ and an error in the solution of the electric potential of $\varepsilon_{\Phi} \approx 10^{-9}$. The results from Fig. 5 show no deviation in the lateral directions *y* and *z*, which aligns with the chosen boundary conditions. Since the electric potential exhibits a linear progression as already presented before, the current in the *x*-direction is constant throughout the whole computational domain as depicted in Fig. 5a. Fig. 5b verifies that the current in the *x*-direction is also constant at the contact interface. In addition, due to the linear course of the displacement in the *x*-direction as shown before, the *xx*-component of the Cauchy stress is constant as displayed in Fig. 5c, where the *xx*-component of the Cauchy stress is calculated using $\boldsymbol{e}_x \cdot \boldsymbol{\sigma} \cdot \boldsymbol{e}_x$ with the unit vector in the *x*-direction $\boldsymbol{e}_x$. Finally, Fig. 5d demonstrates that the *xx*-component of the Cauchy stress is also constant across the complete contact interface. The fluxes across the contact interface are constant in the lateral direction because we used a segment-based coupling scheme. This is not necessarily true for collocation-based schemes like the node-to-segment method, as shown for lithium-ion batteries with liquid electrolytes in Ref. 46.

*Conservation of mass.*—The second step in verifying the presented model is performed by showing that the coupled electro-chemo-mechanics problem, including the *contact* formulation at the interface between the cathode and electrolyte, fulfills the conservation of mass. Therefore, we introduce a simplified geometry of an SSB consisting of a lithium metal anode (gray), a solid electrolyte (green), and one cathode active material particle (anthracite) as shown in Fig. 6. The dimensions of the geometry and quantities of the discretization are listed in Table B·IV. Coreform Cubit[47] is used to obtain a finite element mesh consisting of tetrahedral elements with linear shape functions. The presented geometry is prestressed to a stack pressure of 70 MPa by a Robin-type boundary condition (see Eq. 36) applied to $\Gamma_a$ approximating the stiffness of the surrounding devices by a spring in a prestressed state. Then, we perform a charging process at a C-rate of 0.1 C from the fully discharged state until the cutoff voltage of 4.2 V is reached. The mechanical prestress (see Eq. B·6) and the charging current (cf Eq. B·7) are ramped up to avoid oscillations. Fig. 7 shows the development of the amount of substance of lithium and lithium-ions in the different parts of the battery over the state of charge throughout the charging process. As expected, the amount of substance of lithium linearly increases inside the anode, whereas it linearly decreases inside the active material of the cathode due to the constant current charging. Furthermore, the amount of substance of lithium-ions remains constant in the solid electrolyte. Moreover, the total amount of substance of lithium and lithium-ions remains constant in the battery cell with only a minor relative deviation of approximately $10^{-5}\%$. The discrete solution does not perfectly fulfill the mass conservation due to the highly nonlinear nature of Eqs. 7 and 8. However, we already showed in our previous work[35] that the model formulation is consistent, and the error decreases as the time discretization is refined.
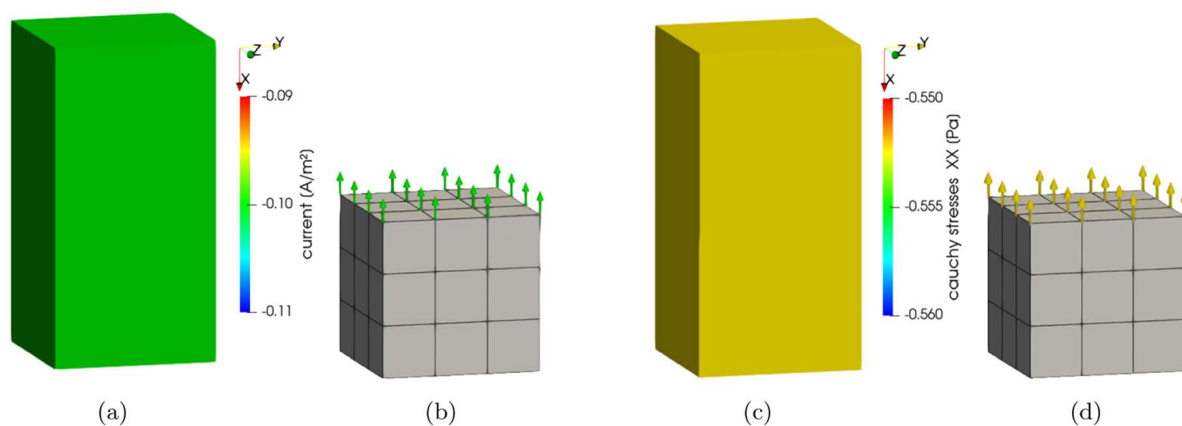
**Figure 5.** Results of the patch test for the presented model including the *contact* interface formulation. (a) shows the current in the *x*-direction and (b) the current in the *x*-direction at the contact interface. The *xx*-component of the Cauchy stress is displayed in (c), and the *xx*-component of the Cauchy stress at the contact interface in (d).
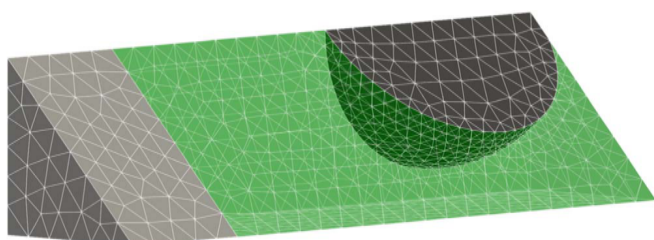


**Figure 6.** Simplified SSB geometry consisting of a lithium metal anode (gray), a solid electrolyte (green), and a cathode active material particle (anthracite).
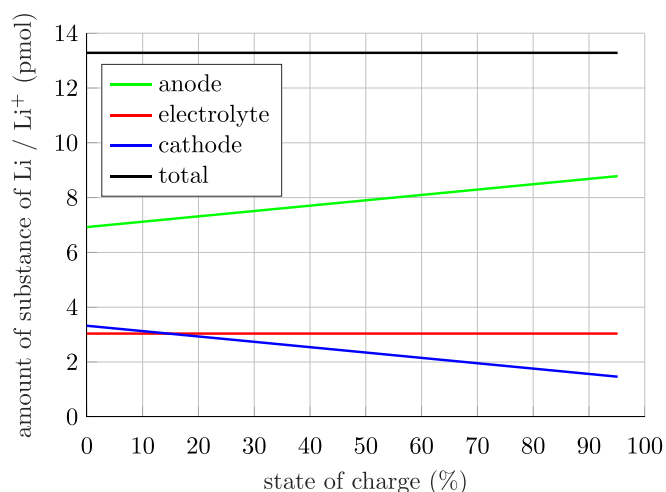


**Figure 7.** Amount of substance of lithium and lithium-ions over the state of charge during charging at 0.1 C until the cutoff voltage of 4.2 V is reached.

***Influence of different mechanical stack pressures.***—The influence of different external mechanical stack pressures during cycling combined with the distinct interface models *mesh tying* and *contact* is analyzed. Therefore, we use the simplified geometry as shown in Fig. 6 assembled in a completely discharged state, apply a mechanical stack pressure of either 50, 60, or 70 MPa to the system, and perform a charging process at a C-rate of 0.1 C until the cutoff voltage of 4.2 V is reached. Again, the mechanical prestress (see Eq. B·6) and the charging current (cf Eq. B·7) are ramped up to avoid oscillations. The resulting cell voltage curves over the state of charge (SoC) of the battery cell are depicted in Fig. 8. Comparing
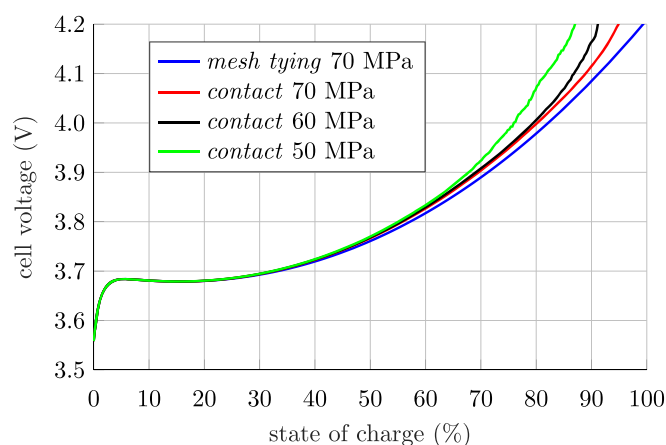


**Figure 8.** Comparison of the cell voltage curves over the state of charge of the different mechanical interface models for different mechanical stack pressures.

the *mesh tying* and *contact* interface models for the same mechanical stack pressure of 70 MPa reveals that neglecting the physical effect of delaminations at the interface of active material and solid electrolyte leads to overestimating the transferred charge. This is in line with our expectation, as the delaminated parts of the interface do not take part in the charge transfer anymore. Consequently, the current at the remaining, not delaminated interface area increases. This effect leads to a rising internal resistance of the cell, and the cutoff voltage is reached earlier. A comparison of the three different progressions for the *contact* interface model shows that a higher mechanical stack pressure increases the transferred charge of the charging process. Since the dominant electro-chemo-mechanical interaction effect in this study is the delamination at the interface of active material and solid electrolyte, the simulation result for the *mesh tying* interface model can be interpreted as the extreme case where no delamination occurs. The results of the *contact* interface model would converge to the result of the *mesh tying* interface model for increasing mechanical stack pressure. Fig. 9 supports that the relevant effect for the differences is the delamination at the interface. It shows the share of the total cathode interface area that is delaminated, i.e. not in contact with the adjacent solid electrolyte, over the state of charge of the cell. Comparing the *contact* interface model for different mechanical stack pressures indicates that for a larger stack pressure, the delamination occurs at a later SoC and that the share of the delaminated interface area is always lower. This effect can be directly attributed to the higher mechanical stack
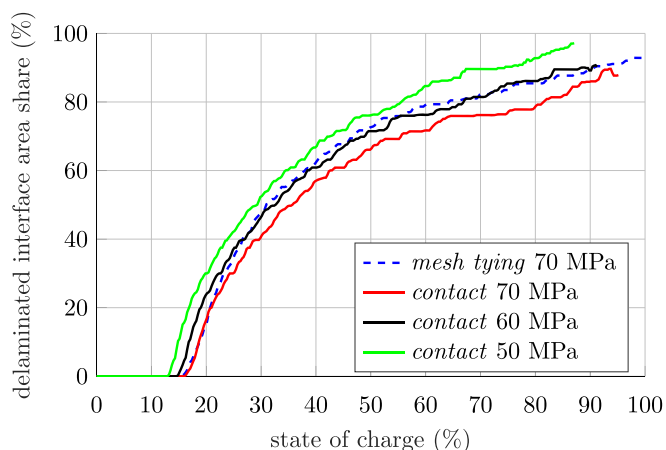
**Figure 9.** Comparison of the delaminated cathode-solid electrolyte interface area share over the state of charge of the different mechanical interface models for different mechanical stack pressures.

pressure, as this leads to a higher level of compressive stress, which must be compensated by the volume change in the active materials before delamination occurs. The progression of the *mesh tying* simulation is depicted with a dashed line as in this scenario no real delamination occurs by construction of the interface model. However, the mechanical interface stress can be post-processed and used to quantify the share of the cathode interface under tensile stress that would lead to delaminations if not suppressed by the interface model formulation. The *mesh tying* simulation at 70 MPa shows an almost identical progression to the corresponding *contact* simulation at the beginning. Yet, starting from an SoC of approximately 25%, it exhibits almost the same course as the *contact* scenario for a mechanical stack pressure of 60 MPa. This highlights that the mechanical interface law also impacts the solution of the solid mechanics field even in such a simple artificial setup, leading to an overestimation of the interface share between the active material and solid electrolyte experiencing tensile stress. In Fig. 10, we compare the concentration distribution inside the composite cathode active material particle for the *mesh tying* and *contact* interface model of the simulations performed at a mechanical stack pressure of 70 MPa. Furthermore, black arrows are inserted at the interface of the cathode active material and solid electrolyte to visualize a normalized local charge flux density. The presented instants in time represent the state at 20% and 50% SoC, as well as the final state when the cutoff voltage of 4.2 V is reached. For the *mesh tying* simulations in Figs. 10a, 10c and 10e, we observe a mainly radial concentration gradient throughout the simulation time with a minor deviation toward the axial direction mainly visible at 20% SoC. Moreover, the black arrows indicate that the local charge flux



(a) *mesh tying* model at 20% SoC



(b) *contact* model at 20% SoC



(c) *mesh tying* model at 50% SoC



(d) *contact* model at 50% SoC



(e) *mesh tying* model at 4.2 V ≈ 99.4% SoC



(f) *contact* model at 4.2 V ≈ 94.9% SoC

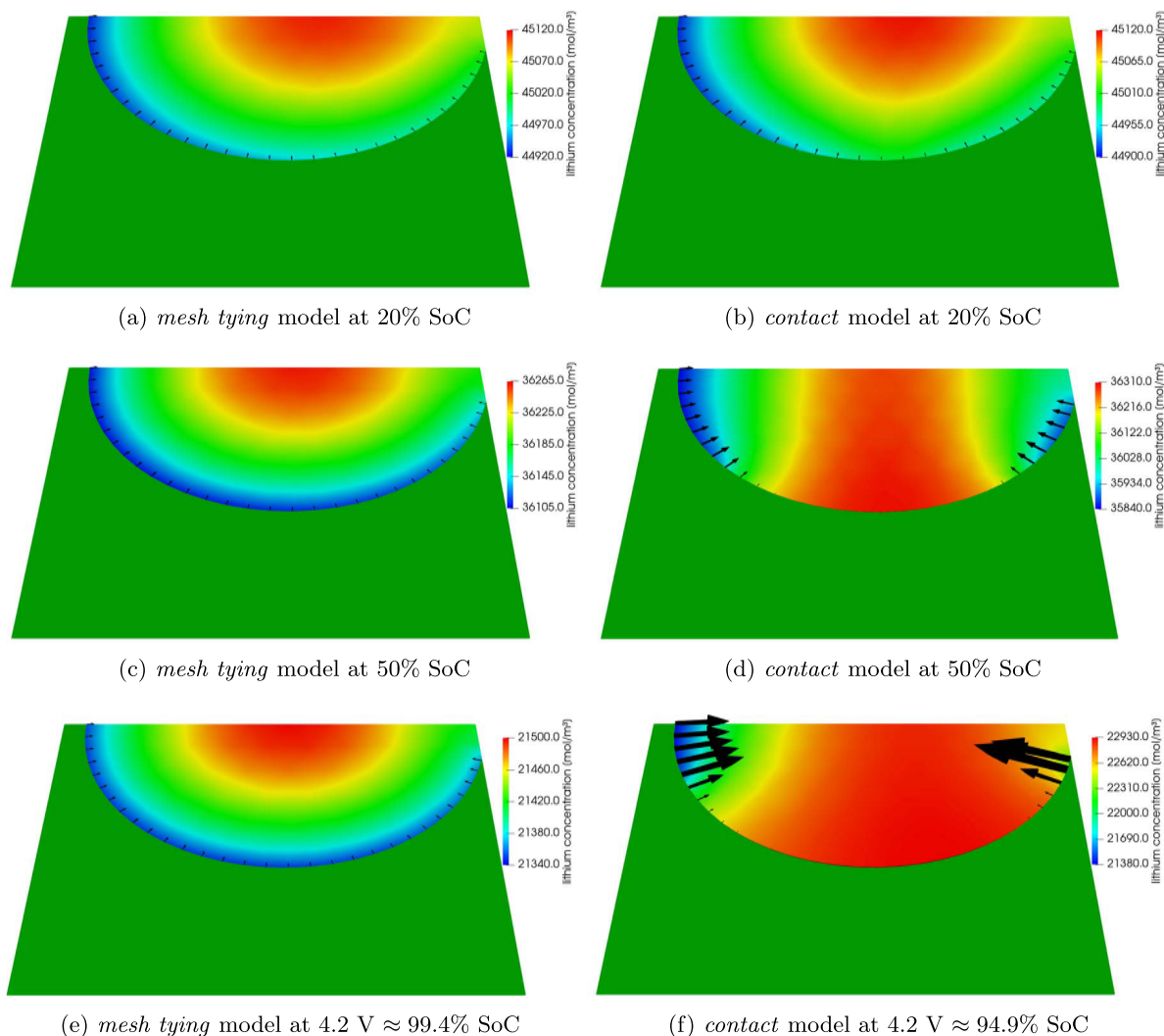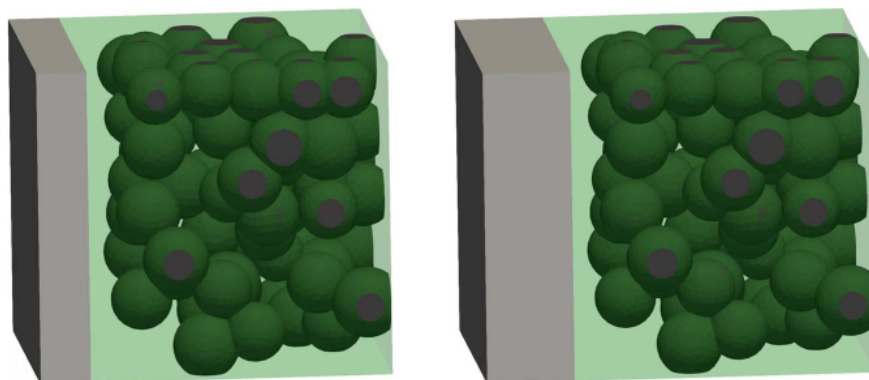**Figure 10.** Comparison of the development of the concentration distribution in the cathode active material at different states of charge for the *mesh tying* and the *contact* interface model for a mechanical stack pressure of 70 MPa. Note that each figure has its separate color bar. The black arrows indicate the magnitude of the local charge flux density across the cathode-solid electrolyte interface.

(a) assembled in discharged state  (b) assembled in charged state

**Figure 11.** Complex SSB geometries consisting of a lithium metal anode (gray), a separator and catholyte made of solid electrolyte (green), and an artificial cathode active material particle microstructure (anthracite).

density remains homogeneously distributed across the complete cathode-solid electrolyte interface during the simulation. While the concentration distribution looks almost identical for the *contact* interface model at the beginning of the simulation, when no delamination has occurred yet, the concentration distribution completely changes for the later instances in time. The delamination of active material and solid electrolyte first occurs in lateral directions near the middle of the particle. This is indicated by the locally disappearing interface charge flux, represented by the vanishing black arrows (see Fig. 10d). Since charge conservation still has to be fulfilled, this is compensated by a larger interface charge flux in the remaining interface area, as depicted by the increasing size of the black arrows near the current collector and the separator. Finally, Fig. 10f shows that the delaminated area has further increased, as depicted by the even larger black arrows symbolizing the local charge flux density confined to an even smaller interface area. This series of pictures shows that the mechanical interface model can largely affect the charge and discharge behavior of the active material if a partial delamination at the interface of active material and solid electrolyte occurs.

***Investigations on complex microstructures.***—In this section, we show the influence of the mechanical interface model on the simulation results of complex microstructures. Therefore, two complex microstructures of an SSB, each consisting of a lithium metal anode (gray), a solid electrolyte (green), and an artificially created cathode active material microstructure whose particle size distribution is parameterized using a log-normal distribution (anthracite) as shown in Fig. 11 are introduced. Please note that due to the representation of the electrolyte as a transparent body, the surfaces of the cathode active material inside the solid electrolyte are depicted in dark green. The first microstructure displayed in Fig. 11a represents an SSB cell that is assembled in the discharged state, i.e. with lithiated cathode active material, whereas the second microstructure displayed in Fig. 11b represents an SSB cell assembled in the charged state, i.e. with delithiated cathode active material and a thicker lithium metal anode to keep the total lithium inventory constant in both cases. The geometric dimensions, the parameterization of the log-normal size distribution of the cathode active material particle diameters, and quantities of the discretization for both cases are listed in Table B·IV. We use Coreform Cubit[47] to obtain a finite element mesh of tetrahedral elements with linear shape functions. In the following, we analyze the critical load cases for both variants, i.e. the first charge process for the microstructure assembled in the discharged state and the first discharge process for the microstructure assembled in the charged state.

*Charge process of a cell assembled in discharged state.*—The simulations start with applying a mechanical stack pressure of 70 MPa of the cell assembled in a fully discharged state as shown in Fig. 11a. When the stack pressure is reached, a charging process at a
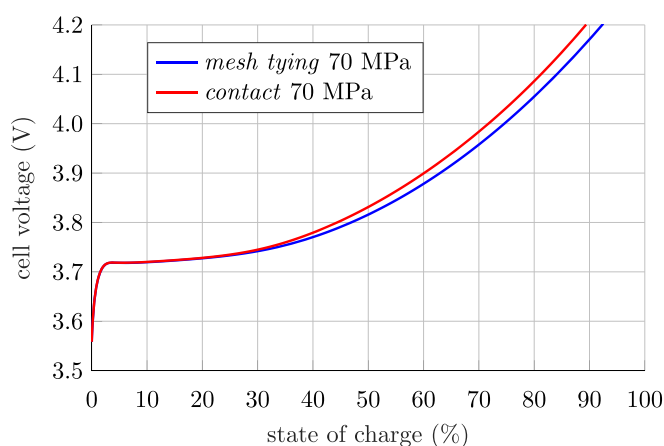


**Figure 12.** Comparison of the cell voltage curves over the state of charge for two different mechanical interface models during a charging process applied to a complex microstructure of a cell assembled in the discharged state.

C-rate of 0.5 C until a cutoff voltage of 4.2 V is performed. The mechanical stack pressure (see Eq. B·6) and the charging current (cf Eq. B·7) are ramped up to avoid oscillations. Again, we compare the results of the *mesh tying* and *contact* interface model. Fig. 12 shows the cell voltage over the state of charge of the cell for the simulations performed with the two different interface models. The *contact* simulation shows a higher course of the cell voltage over SoC starting from about 30% SoC. This difference in the cell voltage indicates a higher internal resistance which we attribute to delaminations at the interface of active material and solid electrolyte. Furthermore, the curve for the *contact* simulation has a higher slope so that the two curves gradually move away. In this scenario, the transferred charge is again overestimated if delamination effects are neglected, leading to an SoC of 92.5% in the *mesh tying* case. In contrast, an SoC of only 89.4% is reached for the model incorporating the delamination effect. In Fig. 13, the concentration distribution for the two different interface models is compared at two instants in time. In the *mesh tying* case, the concentration gradient is mainly oriented in the axial direction, with the smallest concentration value near the anode on the left. In addition, there is a subordinate tendency of the concentration gradient in the radial direction of the active material particles because the particles are always in contact with the surrounding electrolyte, and a charge exchange can occur over their entire surface throughout the charging process. For the *contact* scenario, the concentration distribution looks entirely different as local delaminations dominate it. Due to the applied axial load, the delaminations occur mainly in lateral directions. Therefore, the axial dependency of the concentration distribution is even enhanced compared to the *mesh tying* case. In
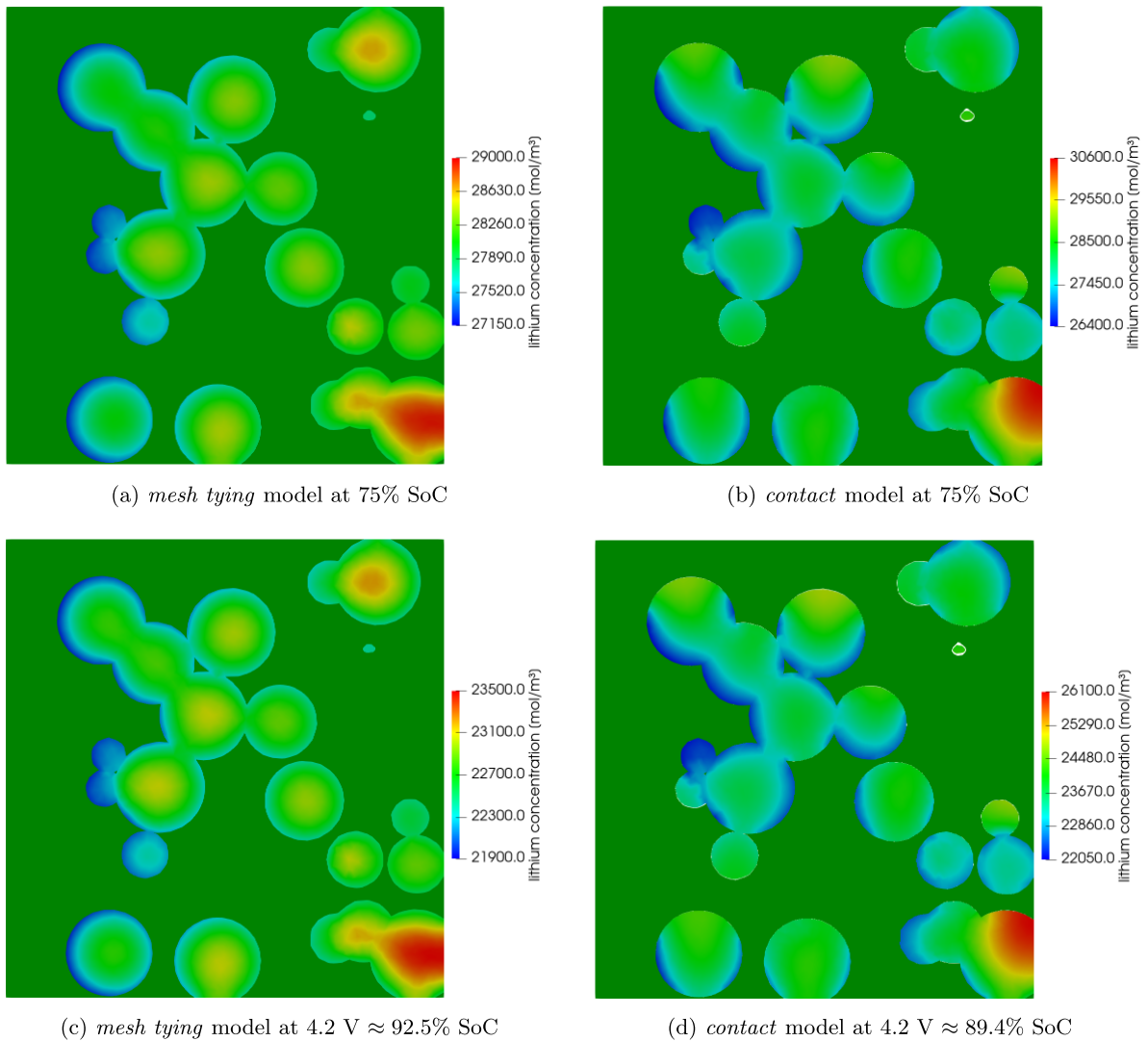
(a) *mesh tying* model at 75% SoC



(b) *contact* model at 75% SoC



(c) *mesh tying* model at 4.2 V ≈ 92.5% SoC



(d) *contact* model at 4.2 V ≈ 89.4% SoC

**Figure 13.** Comparison of the concentration distribution in the cathode active material at different states of charge for the *mesh tying* and the *contact* interface model on a slice through the complex microstructure of a cell assembled in the discharged state. Note that each figure has its color bar.

contrast, the concentration gradient in the radial direction of the cathode active material has vanished. This leads to a more inhomogeneous concentration distribution for the *contact* interface model, resulting in a lower SoC at the end of the charge process.

The most likely cause of the local delaminations at the interface of cathode particles and solid electrolyte is the cell assembly in the discharged state, i.e. with lithiated cathode active material, as the cathode particles shrink in volume during the charging process, i.e. during delithiation. Even with a mechanical stack pressure of 70 MPa, the used electrolyte cannot compensate for this volume change through mechanical deformation. Therefore, delamination occurs at the interface of active material and solid electrolyte, leading to a deteriorated charging performance.

Lastly, the validity of the assumption that the influence of adhesion effects on the delamination at the solid-solid interface of active material and solid electrolyte inside the composite cathode is negligible is verified. Therefore, the stresses at the interface during the charging process for the *mesh tying* interface model are evaluated. As already discussed in the introduction, we expect the value for the adhesion strength of 412 kPa reported in Ref. 28 to be the most relevant as the material system is closest to the one investigated in this work. However, for checking the validity of the assumption we use the largest reported value of the adhesion strength in the literature of 8 MPa to obtain a worst-case estimate. Fig. 14 depicts the progression of the interface area share of the
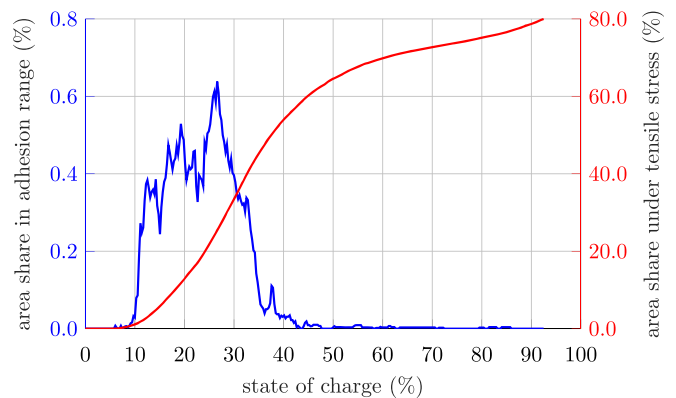


**Figure 14.** Development of the interfacial area share under tensile stresses and the interfacial area share that experiences tensile stresses in a range relevant for adhesion effects, i.e. up to 8 MPa, at the cathode active material-solid electrolyte interface for the *mesh tying* interface model.

interface between the cathode active material and the solid electrolyte over the state of charge that experiences tensile stresses up to 8 MPa. According to the worst-case estimate of the adhesion strength deduced from the literature, this is the range of tensile stresses for which

**Figure 15.** Comparison of the cell voltage curves over the state of charge for the different mechanical interface models during a discharging process applied to a complex microstructure of a cell assembled in the charged state.

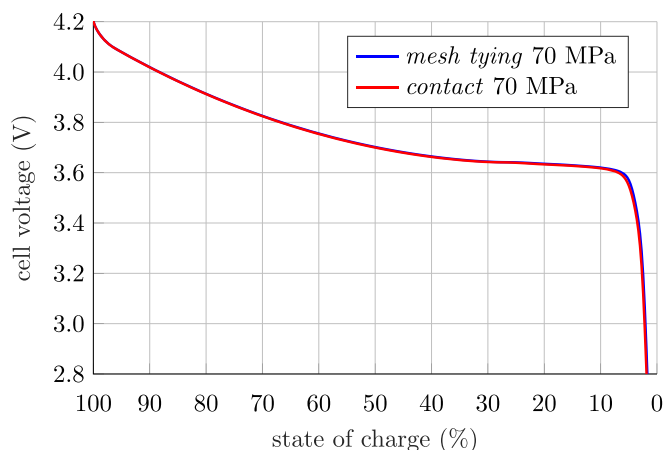adhesion effects would be relevant. The plot shows that this share is always below 0.7% of the total interface area. Furthermore, it illustrates the share of the interfacial area that experiences tensile stresses, which goes up to 80% of the total interface area. In conclusion, this exhibits that a large part of the interface experiences tensile stresses exceeding the adhesion strengths, supporting that the effect of adhesion can be neglected.

*Discharge process of a cell assembled in charged state.*—To further substantiate the previous finding that a cell assembly in the discharged state can be problematic w.r.t. delaminations, we now investigate the second cell which is assembled in a charged state as presented in Fig. 11b. The simulations start from a fully charged state with applying a mechanical stack pressure of 70 MPa. Once the stack pressure is reached, we discharge at a C-rate of 0.5 C until a cutoff voltage of 2.8 V. To avoid oscillations, the stack pressure (see Eq. B·6) and the charging current (cf Eq. B·7) are ramped up. Fig. 15 depicts the cell voltage curves over the state of charge of the cell throughout the discharge process. Only a minor difference toward the end of the discharge process at about 6% SoC is observed. The remaining SoC when the cutoff voltage of 2.8 V is reached is approximately 1.7% in the *mesh tying* case and 1.9% in the *contact* case, thus only deviating by 0.2%. This indicates that in

contrast to the previously investigated setup, no significant delaminations occur in this scenario. Again, this is verified by analyzing the concentration distribution in a slice at the end of the discharge process as depicted in Fig. 16. We see minor differences in the concentration distribution obtained by the simulations using the two different interface models. As already expected from the observation of the cell voltage, the concentration distributions for both cases show clear similarities. In both cases, the concentration gradient is predominantly oriented in the radial direction of the active material particles. There are also no clear indications of local delaminations that would result in significantly changed concentration profiles, as observed for the previously analyzed cell that is assembled in the discharged state. This confirms the hypothesis from the previous Section that a cell assembly in the discharged state can increase mechanical problems, as the tendency of delamination at the interface of the solid electrolyte and cathode active material is increased.

**Summary**

We present a novel approach to incorporate the effect of delamination and possible recontacting at the internal interfaces of three-dimensional resolved microstructures of solid-state batteries. The proposed model can spatially resolve local delaminations by consistently enforcing the constraints originating from contact mechanics using Nitsche's method. It accounts for the conservation of charge, mass, and momentum to model the interaction of electrochemistry and solid mechanics while being capable of capturing large deformations originating from, e.g., lithiation-dependent volume changes of the active materials. After successfully verifying the model, we apply it to different scenarios to analyze the interaction of electrochemistry and solid mechanics while accounting for delaminations. We show that an increased mechanical stack pressure leading to higher compressive stresses inside the battery reduces the tendency for delaminations at the interface of active material and solid electrolytes. As reported in the literature, the simulations reveal that delaminations result in higher internal resistance and lower transferred charge when performing constant current charging. Moreover, we show that adhesion effects do not play a significant role in preventing delaminations at the interface between cathode active material and solid electrolyte for the investigated scenarios. Furthermore, we analyze two different cell concepts, namely, one assembled in a discharged state, i.e. with lithiated cathode active material, and another assembled in a charged state, i.e. with delithiated cathode active material. The simulations demonstrate

(a) *mesh tying* model at 2.8 V ≈ 1.7% SoC

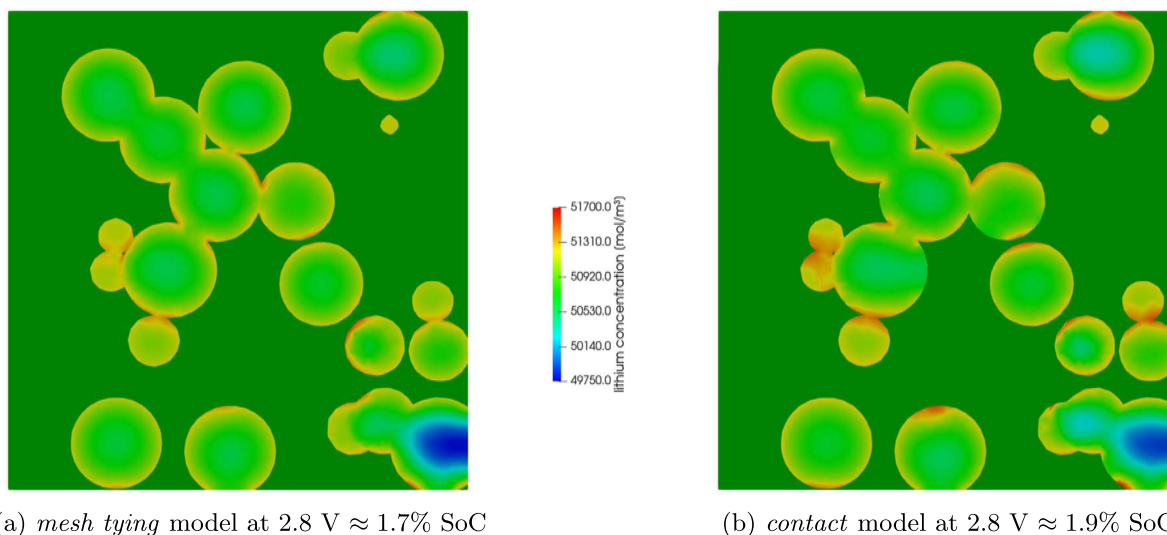(b) *contact* model at 2.8 V ≈ 1.9% SoC

**Figure 16.** Comparison of the concentration distribution at the end of the discharge process for the *mesh tying* and the *contact* interface model on a slice through the complex microstructure of a cell assembled in the charged state.

that assembling the cell in a discharged state, which is considered optimal from energy and power density considerations as an excess lithium metal anode can be prevented in theory, leads to an increased tendency for delaminations at the interface of cathode active material and solid electrolyte. This can be attributed to the effect that the volume of the active material shrinks upon charging the cell, i.e. delithiation of the cathode active material NMC622. At least for the investigated material combinations, this leads to delaminations at the interface and, consequently, higher internal resistance and less transferred charge as theoretically possible.

For future work, we propose incorporating the inhomogeneous growth of the lithium metal anode caused by inhomogenous plating currents at the interface of the lithium metal anode and solid electrolyte. Combined with the proposed contact interface treatment and elaborate constitutive models for the visco-plastic behavior of lithium, the delamination behavior on the anode side could be analyzed in detail. Furthermore, an extension of the contact interface model by adhesive effects can be of interest, especially for sintered oxide-based composite electrodes, to enable the detailed analysis of such systems. Moreover, based on the proposed model, cell concepts can be analyzed and optimized w.r.t. the required external mechanical pressure during operation.

## Data Availability

The result data of the simulations is made available via the Zenodo record 10.5281/zenodo.13802728.

## Appendix A. Details on the Choice of Nitsche Contact Parameters

***Estimation of the penalty parameter.***—The choice of the penalty parameter $\gamma_n$ contained in the weak form of the contact constraint in Eq. 46 is so far unspecified. It is known that the penalty parameter needs to scale with the material stiffness and the inverse of the mesh size to ensure coercivity.[48] Moreover, small penalty parameters are favorable in nonlinear contact problems due to the non-smoothness of the boundary integral term in Eq. 46. The non-smoothness originates from the involved minimum function (cf Eq. 45) that switches the penalty term on or off. Especially for large penalty parameters, this non-smoothness can severely deteriorate the convergence behavior of the nonlinear solver, i.e. the Newton–Raphson method in our case. Furthermore, Ref. 48 analyzed for linear kinematics that the variant $\theta = 0$ requires a lower bound for the penalty parameter $\gamma_n > C_u$ to ensure coercivity. An estimate of the constant $C_u$ can be obtained from the eigenvalue problem

$$\boldsymbol{A}\boldsymbol{v} = \lambda \boldsymbol{B}\boldsymbol{v}. \qquad \text{[A·1]}$$

We choose the matrices $\boldsymbol{A}$ and $\boldsymbol{B}$ as suggested in Ref. 49

$$\boldsymbol{A} = \int_{\Gamma_{\text{ct}}} \left( (\boldsymbol{F} \otimes \boldsymbol{N}) : \mathbb{C} : \frac{\partial \boldsymbol{E}}{\partial \boldsymbol{u}} \right)^{\text{T}} \cdot \left( (\boldsymbol{F} \otimes \boldsymbol{N}) : \mathbb{C} : \frac{\partial \boldsymbol{E}}{\partial \boldsymbol{u}} \right) d\Gamma, \qquad \text{[A·2]}$$

$$\boldsymbol{B} = \int_{\Omega_{\text{ct}}} \left( \frac{\partial \boldsymbol{E}}{\partial \boldsymbol{u}} \right)^{\text{T}} : \mathbb{C} : \left( \frac{\partial \boldsymbol{E}}{\partial \boldsymbol{u}} \right) d\Omega, \qquad \text{[A·3]}$$

with the nonlinear elasticity tensor $\mathbb{C} = \frac{\partial^2 \Psi}{\partial \boldsymbol{E} \partial \boldsymbol{E}}$, the Green–Lagrange strain tensor $\boldsymbol{E} = \frac{1}{2}(\boldsymbol{C} - \boldsymbol{I})$, the right Cauchy–Green tensor $\boldsymbol{C} = \boldsymbol{F}^{\text{T}} \cdot \boldsymbol{F}$, and the second order identity tensor $\boldsymbol{I}$. The eigenvalue problem contains all elements in the discrete problem intersecting the contact boundary, which is indicated by $\Omega_{\text{ct}}$. According to Ref. 50 the required constant is obtained as the maximum eigenvalue $C_u = \lambda_{\text{max}}$. Dolbow and Harari show in Ref. 51 that solving the eigenvalue problem at the complete contact interface is unnecessary to obtain stability. Instead, it is enough to calculate piecewise constant values $C_{u,e}$ for each discrete element $e$ intersecting the contact interface determined by the corresponding local eigenvalue problem. The local penalty parameter for each element is then calculated using a reference penalty parameter $\gamma_{\text{n,0}}$ as

$$\gamma_{\text{n,e}} = C_{u,e} \, \gamma_{\text{n,0}}. \qquad \text{[A·4]}$$

***Choice of the weighting factor.***—The last parameter to define is the weighting factor $\omega_s$. Especially when the stiffness of the body $\Omega^{(1)}$ is much larger compared to the stiffness of $\Omega^{(2)}$, a fixed one-sided weighting, e.g. by applying $\omega_s = 1$, can lead to large penalty parameters determined by the procedure described in the previous section.. As shown in Ref. 52 this can even affect the quality of the solution. The so-called harmonic weights are introduced in Ref. 53 for such scenarios and applied in this work. The weight between an element of body (1) and an element of body (2) is calculated using the constants obtained from the local eigenvalue problem in Eq. A·1 as

$$\omega_s = \frac{C_u^{(2)}}{C_u^{(1)} + C_u^{(2)}}. \qquad \text{[A·5]}$$

## Appendix B. Model Parameters

The model parameters used to perform the simulations are presented in this section. The parameters required to define the solid mechanics problem of the SSB are given in Table B·I. The parameters for the governing equation describing the electrochemical behavior are listed in Table B·II.

The following equation defines the open circuit voltage $\Phi_0$ of the cathode material NMC622 against lithium depending on the lithiation state $\chi = c \, \chi_{\text{max}} \det(\boldsymbol{F})/c_{\text{max}}$, where the maximum concentration of lithium inside the electrode is denoted by $c_{\text{max}}$ and the corresponding lithiation state by $\chi_{\text{max}}$ based on Ref. 61

$$
\begin{aligned}
\Phi_0(\chi) = {}& 13.4905 - 10.96038\,\chi + 8.203\,617\,\chi^{1.358699} \\
& - 3.107\,58 \cdot 10^{-6} \exp(127.1216\,\chi - 114.2593) \\
& - 7.033\,556\,\chi^{-0.03362749}. \qquad \text{[B·1]}
\end{aligned}
$$

Moreover, the lithiation-dependent volume change of the active materials is parameterized as given in Table B·III. In this work, two different lithiation-dependent volume change laws as presented in Eqs. 9 and 10 are applied. To parameterize the cathode active material growth law, the polynomial $f(\chi) = \sum_{i=0}^{7} a_i \chi^i$ is used. Fig. 17 visualizes the volumetric change of the NMC622 active material as a function of the lithiation state $\chi$. The geometric dimensions as well as the quantities of the discretization for the investigated geometries are listed in Table B·IV. For the complex geometry, the diameter distribution is parameterized using a log-normal distribution:

$$f(\bar{d}|\mu, \sigma) = \frac{1}{\bar{d}\sigma\sqrt{2\pi}} \exp\left( \frac{-(\log \bar{d} - \mu)^2}{2\sigma^2} \right) \quad \text{for } \bar{d} > 0, \qquad \text{[B·4]}$$

**Table B·I. Mechanical parameters.**

| Parameter | Value | Unit | Description | Source |
|---|---|---|---|---|
| | | Cathode: NMC622 | | |
| E | $1.75 \cdot 10^{11}$ | Pa | Young's modulus | 54 |
| $\nu$ | 0.3 | — | Poisson's ratio | 55–57 |
| $\rho$ | $5.03 \cdot 10^{3}$ | $\frac{kg}{m^3}$ | density | 35 |
| | | Electrolyte: $\beta$-LPS | | |
| E | $2.89 \cdot 10^{10}$ | Pa | Young's modulus | 58 |
| $\nu$ | 0.27 | — | Poisson's ratio | 58 |
| $\rho$ | $1.88 \cdot 10^{3}$ | $\frac{kg}{m^3}$ | density | 59 |
| | | Anode: lithium | | |
| E | $4.90 \cdot 10^{9}$ | Pa | Young's modulus | 26 |
| $\nu$ | 0.42 | — | Poisson's ratio | 26 |
| $\rho$ | $5.34 \cdot 10^{2}$ | $\frac{kg}{m^3}$ | density | 60 |
| | | Mechanical prestress boundary condition: Eq. 36 | | |
| k | $1.0 \cdot 10^{13}$ | $\frac{kg}{m^2 s^2}$ | equivalent spring stiffness | assumed |

**Table B·II. Electrochemical material parameters.**

| Parameter | Value | Unit | Description | Source |
|---|---|---|---|---|
| | | Cathode: NMC622 | | |
| $\sigma$ | $4.55 \cdot 10^{-1}$ | $\frac{S}{m}$ | electronic conductivity | averaged from 25 |
| D | $2.40 \cdot 10^{-14}$ | $\frac{m^2}{s}$ | diffusion coefficient | averaged from 25 |
| $\Phi_0$ | Eq. B·1 | V | open circuit potential | 61 |
| $i_0$ | 4.98 | $\frac{A}{m^2}$ | exchange current density factor | adapted from 25 |
| $\alpha_a$ | 0.5 | — | anodic symmetry coefficient | 25 |
| $c_{max}$ | $5.19 \cdot 10^{4}$ | $\frac{mol}{m^3}$ | maximum concentration | 25 |
| $\chi_{max}$ | 1.0 | — | maximum lithiation state | 25 |
| $\chi_{0\%}$ | 1.0 | — | lithiation state at 0% SoC | assumed |
| $\chi_{100\%}$ | $4.04 \cdot 10^{-1}$ | — | lithiation state at 100% SoC | assumed |
| | | Electrolyte: $\beta$-LPS | | |
| $\kappa$ | $1.20 \cdot 10^{-2}$ | $\frac{S}{m}$ | ionic conductivity | 25 |
| $t_{el}$ | 1.0 | — | lithium-ion transference number | 25 |
| | | Anode: lithium | | |
| $\sigma$ | $1.00 \cdot 10^{5}$ | $\frac{S}{m}$ | electronic conductivity | 25 |
| $\Phi_0$ | 0.0 | V | open circuit potential | 25 |
| $i_0$ | 8.87 | $\frac{A}{m^2}$ | exchange current density factor | 25 |
| $\alpha_a$ | 0.5 | — | anodic symmetry coefficient | 25 |

with the mean $\mu$ and standard deviation $\sigma$ of the normally distributed logarithm of the variable. As the log-normal distribution is unit-less, the unit of the diameter $d$ is retained by $\bar{d} = d/1\mu$ m.

**Table B·III. Parameters of the volume change laws.**

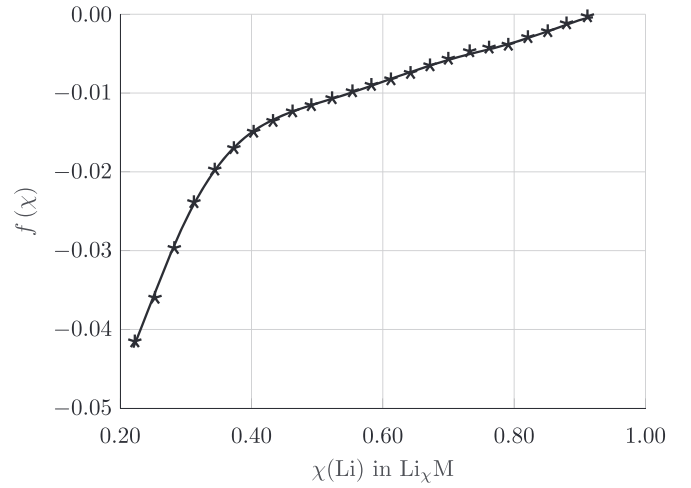| Parameter | Value | Unit |
|---|---|---|
| | Cathode: NMC622 | |
| $a_0$ | 0.000444 577 043 098 | — |
| $a_1$ | −1.24116361022373 | — |
| $a_2$ | 9.304 619 097 348 83 | — |
| $a_3$ | −29.44977325195 | — |
| $a_4$ | 49.112 683 877 260 3 | — |
| $a_5$ | −45.1097641074935 | — |
| $a_6$ | 21.599 436 266 847 1 | — |
| $a_7$ | −4.21656846170118 | — |
| | Anode: lithium | |
| g | $1.2998 \cdot 10^{-5}$ | $\frac{m^3}{mol}$ |



**Figure 17.** Approximation of measured data of the volume change of NMC622 as published in Ref. 26 (symbols) by a polynomial fit of order seven (solid lines).

The initial conditions for the mass conservation are given in Table B·V, where the initial concentration of the lithium metal anode is calculated based on the assumption of a pure substance from:

$$c = \frac{\rho}{M}. \qquad [\text{B·5}]$$

Finally, the mechanical prestress and the C-rate are ramped up to prevent oscillations. We first gradually increase the mechanical prestress to the desired level by adapting the spring displacement offset in normal direction $u_k$ (cf Eq. 36) using

$$u_k = u_{k,\text{target}}\left(-0.5\left[1 + \cos\left(\frac{t\,\pi}{250\text{ s}}\hat{C}\right)\right]\mathcal{H}\left(\frac{250\text{ s}}{\hat{C}} - t\right) + 1\right)$$

for $t \geqslant 0$,

$$[\text{B·6}]$$

with the spring displacement target value $u_{k,\text{target}}$, the applied C-rate $\hat{C} \in \{0.1, 0.5\}$ in the shown examples and the heaviside function $\mathcal{H}$. To obtain the mechanical prestress the required spring displacement target values are listed in Table B·VI.

Once the complete mechanical prestress is established, the (dis-) charge C-rate $C$ is ramped up in the same timespan $t_{\text{ramp}} = \frac{250\text{ s}}{\hat{C}}$ as the mechanical prestress before by employing

**Table B·IV. Geometric dimensions and quantities of the discretization.**

| Quantity | Unit | Simplified geometry | Complex geometry |
|---|---|---|---|
| lateral dimensions | $\mu$m | — | 50.0 |
| thickness composite cathode | $\mu$m | 10.0 | 40.0 |
| thickness solid electrolyte separator | $\mu$m | 10.0 | 8.0 |
| thickness anode (discharged / charged) | $\mu$m | 5.0 | 8.0 / 14.0 |
| volume share of active material and electrolyte in cathode | — | 36:64 | 38:62 |
| $\mu$ of log-normal distribution | — | — | 2.3 |
| $\sigma$ of log-normal distribution | — | — | 0.05 |
| active material particle diameter | $\mu$m | 10.0 | — |
| number of cathode active material particles | — | 1 | 79 |
| number of nodes (discharged / charged) | — | 1, 832 | 106, 716 / 111, 657 |
| number of elements (discharged / charged) | — | 7, 105 | 524, 737 / 553, 356 |

**Table B·V. Initial conditions for the mass conservation.**

| Domain | Initial concentration $c^0$ | Unit | Source |
|---|---|---|---|
| cathode | $2.10 \cdot 10^4$ | $\dfrac{\text{mol}}{\text{m}^3}$ | 25 |
| electrolyte | $1.03 \cdot 10^4$ | $\dfrac{\text{mol}}{\text{m}^3}$ | 25 |
| anode | $7.69 \cdot 10^4$ | $\dfrac{\text{mol}}{\text{m}^3}$ | Eq. B·5 |

**Table B·VI. Spring displacement target values to obtain the desired mechanical prestress.**

| Geometry | Mechanical prestress | Unit | $u_{k,\text{target}}$ | Unit |
|---|---|---|---|---|
| simplified (cf Fig. 6) | $50 \cdot 10^6$ | Pa | $5.041 \cdot 10^{-6}$ | m |
| | $60 \cdot 10^6$ | Pa | $6.049 \cdot 10^{-6}$ | m |
| | $70 \cdot 10^6$ | Pa | $7.057 \cdot 10^{-6}$ | m |
| complex assembled discharged (cf Fig. 11a) | $70 \cdot 10^6$ | Pa | $7.102 \cdot 10^{-6}$ | m |
| complex assembled charged (cf Fig. 11b) | $70 \cdot 10^6$ | Pa | $7.133 \cdot 10^{-6}$ | m |

$$C = \hat{C}\left(-0.5\left[-1 + \cos\left(\frac{t\,\pi}{250\text{ s}}\hat{C} - \pi\right)\right]\mathcal{H}\left(t - \frac{250\text{ s}}{\hat{C}}\right)\right.$$
$$\left. \times\left[1 - \mathcal{H}\left(t - \frac{2\cdot250\text{ s}}{\hat{C}}\right)\right] + \mathcal{H}\left(t - \frac{2\cdot250\text{ s}}{\hat{C}}\right)\right). \qquad \text{[B·7]}$$

Both fields are ramped up depending on the C-rate because the choice of the time step is based on the C-rate, and we thus ensure that their temporal discretization is reasonable.

### ORCID

Christoph P. Schmidt https://orcid.org/0000-0001-8504-9118
Stephan Sinzig https://orcid.org/0000-0002-4951-2993
Wolfgang A. Wall https://orcid.org/0000-0001-7419-3384

### References

1. J. Janek and W. G. Zeier, "A solid future for battery development." *Nat. Energy*, **1**, 16141 (2016).
2. J. Janek and W. G. Zeier, "Challenges in speeding up solid-state battery development." *Nat. Energy*, **8**, 230 (2023).
3. M. J. Wang, R. Choudhury, and J. Sakamoto, "Characterizing the li-solid-electrolyte interface dynamics as a function of stack pressure and current density." *Joule*, **3**, 2165 (2019).
4. T. Krauskopf, H. Hartmann, W. G. Zeier, and J. Janek, "Toward a fundamental understanding of the lithium metal anode in solid-state batteries—an electrochemo-mechanical study on the garnet-type solid electrolyte Li$_{6.25}$Al$_{0.25}$La$_3$Zr$_2$O$_{12}$." *ACS Applied Materials & Interfaces*, **11**, 14463 (2019).
5. J. Kasemchainan, S. Zekoll, D. S. Jolly, Z. Ning, G. O. Hartley, J. Marrow, and P. G. Bruce, "Critical stripping current leads to dendrite formation on plating in lithium anode solid electrolyte cells." *Nat. Mater.*, **18**, 1105 (2019).
6. S. Wang et al., "Influence of crystallinity of lithium thiophosphate solid electrolytes on the performance of solid-state batteries." *Adv. Energy Mater.*, **11**, 2100654 (2021).
7. J. A. Lewis et al., "Linking void and interphase evolution to electrochemistry in solid-state batteries using operando X-ray tomography." *Nat. Mater.*, **20**, 503 (2021).
8. C. Hänsel and D. Kundu, "The stack pressure dilemma in sulfide electrolyte based li metal solid-state batteries: a case study with Li$_6$PS$_5$Cl Solid electrolyte." *Advanced Materials Interfaces*, **8**, 2100206 (2021).
9. R. Koerver, I. Aygün, T. Leichtweiß, C. Dietrich, W. Zhang, J. O. Binder, P. Hartmann, W. G. Zeier, and J. Janek, "Capacity fade in solid-state batteries: interphase formation and chemomechanical processes in nickel-rich layered oxide cathodes and lithium thiophosphate solid electrolytes." *Chemistry of Materials*, **29**, 5574 (2017).
10. S. H. Jung, U. Kim, J. Kim, S. Jun, C. S. Yoon, Y. S. Jung, and Y. Sun, "Ni-rich layered cathode materials with electrochemo-mechanically compliant microstructures for all-solid-state li batteries." *Adv. Energy Mater.*, **10**, 1903360 (2019).
11. T. Shi, Y.-Q. Zhang, Q. Tu, Y. Wang, M. C. Scott, and G. Ceder, "Characterization of mechanical degradation in an all-solid-state battery cathode." *Journal of Materials Chemistry A*, **8**, 17399 (2020).
12. B. Liu, S. D. Pu, C. Doerrer, D. Spencer Jolly, R. A. House, D. L. R. Melvin, P. Adamson, P. S. Grant, X. Gao, and P. G. Bruce, "The effect of volume change and stack pressure on solid-state battery cathodes." *SusMat*, **3**, 721 (2023).
13. H.-K. Tian and Y. Qi, "Simulation of the effect of contact area loss in all-solid-state li-ion batteries." *J. Electrochem. Soc.*, **164**, E3512 (2017).
14. X. Zhang, Q. J. Wang, K. L. Harrison, S. A. Roberts, and S. J. Harris, "Pressure-driven interface evolution in solid-state lithium metal batteries." *Cell Reports Physical Science*, **1**, 100012 (2020).
15. R. A. Ahmed, N. Ebechidi, I. Reisya, K. Orisekeh, A. Huda, A. Bello, O. K. Oyewole, and W. O. Soboyejo, "Pressure-induced interfacial contacts and the deformation in all solid-state Li-ion batteries." *Journal of Power Sources*, **521**, 230939 (2022).
16. Y.-q. Shao, H.-l. Liu, X.-d. Shao, L. Sang, and Z.-t. Chen, "An all coupled electrochemical-mechanical model for all-solid-state Li-ion batteries considering the effect of contact area loss and compressive pressure." *Energy*, **239**, 121929 (2022).
17. B. S. Vishnugopi, K. G. Naik, H. Kawakami, N. Ikeda, Y. Mizuno, R. Iwamura, T. Kotaka, K. Aotani, Y. Tabuchi, and P. P. Mukherjee, "Asymmetric contact loss dynamics during plating and stripping in solid-state batteries." *Adv. Energy Mater.*, **13**, 2203671 (2022) .
19. P. Barai, T. Fuchs, E. Trevisanello, F. H. Richter, J. Janek, and V. Srinivasan, "Study of void formation at the lithium|solid electrolyte interface." *Chemistry of Materials*, **36**, 2245 (2024).
20. P. Barai, T. Rojas, B. Narayanan, A. T. Ngo, L. A. Curtiss, and V. Srinivasan, "Investigation of delamination-induced performance decay at the cathode/LLZO interface." *Chemistry of Materials*, **33**, 5527 (2021).
21. D. Bistri and C. V. D. Leo, "Modeling of chemo-mechanical multi-particle interactions in composite electrodes for liquid and solid-state li-ion batteries." *J. Electrochem. Soc.*, **168**, 030515 (2021).
22. S. Farzanian, J. Vazquez Mercado, I. Shozib, N. Sivadas, V. Lacivita, Y. Wang, and Q. H. Tu, "Mechanical investigations of composite cathode degradation in all-solid-state batteries." *Materials*, **6**, 9615 (2023).